Inorganic Chemistry
Cite This: Inorg. Chem. XXXX, XXX, XXX−XXX
Article
pubs.acs.org/IC

Half-Sandwich Iridium and Ruthenium Complexes: Effective Tracking in Cells and Anticancer Studies

JuanJuan Li,[†] Lihua Guo,[†] Zhenzhen Tian,[†] Shumiao Zhang,[†] Zhishan Xu,[†,‡] Yali Han,[†] Ruixia Li,[†] Yan Li,[†] and Zhe Liu*[,†]

[†]Institute of Anticancer Agents Development and Theranostic Application, The Key Laboratory of Life-Organic Analysis and Key Laboratory of Pharmaceutical Intermediates and Analysis of Natural Medicine, Department of Chemistry and Chemical Engineering, Qufu Normal University, Qufu 273165, People's Republic of China

[‡]Department of Chemistry and Chemical Engineering, Shandong Normal University, Jinan 250014, People's Republic of China

Supporting Information

ABSTRACT: Half-sandwich metal-based anticancer complexes suffer from uncertain targets and mechanisms of action. Herein we report the observation of the images of half-sandwich iridium and ruthenium complexes in cells detected by confocal microscopy. The confocal microscopy images showed that the cyclopentadienyl iridium complex **1** mainly accumulated in nuclei in A549 lung cancer cells, whereas the arene ruthenium complex **3** is located in mitochondria and lysosomes, mostly in mitochondria, although both complexes entered A549 cells mainly through energy-dependent active transport. The nuclear morphological changes caused by Ir complex **1** were also detected by confocal microscopy. Ir complex **1** is more potent than cisplatin toward A549 and HeLa cells. DNA binding studies involved interaction with the nucleobases 9-ethylguanine, 9-methyladenine, ctDNA, and plasmid DNA. The determination of bovine serum albumin binding was also performed. Hydrolysis, stability, nucleobase binding, and catalytic NAD^+/NADH hydride transfer tests for complexes **1** and **3** were also carried out. Both complexes activated depolarization of mitochondrial membrane potential and intracellular ROS overproduction and induced cell apoptosis. Complex **3** arrested the cell cycle at the G_0/G_1 phase by inactivation of CDK 4/cyclin D1. This work paves the way to track and monitor half-sandwich metal complexes in cells, shines a light on understanding their mechanism of action, and indicates their potential application as theranostic agents.

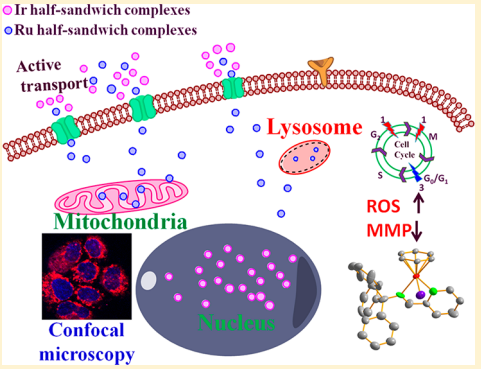

INTRODUCTION

Metal-mediated anticancer drugs have attracted enormous current interest for cancer chemotherapy, since the remarkable discovery of a few platinum-based anticancer drugs, such as cisplatin, carboplatin, and oxaliplatin.[1,2] However, due to the disadvantages of the platinum drugs, such as toxic side effects and platinum drug resistance, the design and discovery of novel non-platinum-based anticancer drugs have received much attention for the therapeutic treatment of cancer.[3−10] Among the transition metals, the two octahedral ruthenium (Ru) complexes NAMI-A and KP1019 have been used for clinical trials.[11,12]

Recently, half-sandwich organometallic low-spin d^6 metal complexes have attracted great interest in chemotherapeutic studies because of their chemical structure diversity and easy control of the hydrophobic nature of the arene or the cyclopentadienyl moiety.[13−15] In addition, the arene and cyclopentadienyl rings displayed significant effects not only on the cellular uptake but also on the function mode toward biological targets and kinetic inertness of the complexes.[16] Sadler et al. established a relationship between the size of the functionalized arene and cyclopentadienyl ligands and anticancer activity for Ru(II) and Ir(III) compounds. The cytotoxicity follows the order tetrahydroanthracene > biphenyl > *p*-cym > benzene > $C_6H_5CO_2CH_2CH_3$ > $C_6H_5CO_2CH_3$ for η^6-arene Ru complexes[17] and Cp^{xbiph} > Cp* for Ir complexes.[16] Very recently, continuously increasing interest has focused on the development of cyclopentadienyl organoiridium anticancer complexes, which showed not only high potency against various cancer cell lines including platinum drug resistant cancer cell lines but also novel mechanism of action.[18−22] However, most of these complexes still suffer from uncertain targets and mechanism of action.

Molecular imaging of metal complexes in cells plays a key role in helping to understand their mechanism of action in many important cellular processes. Cyclometalated iridium or ruthenium complexes have found excellent use as biological and chemical imaging agents and probes by virtue of their intense emission, long emission lifetimes, large Stokes shifts, and high photostability.[23−27] The design and development of fluorescent anticancer complexes is of great significance. The

Received: July 31, 2018

DOI: 10.1021/acs.inorgchem.8b02161
Inorg. Chem. XXXX, XXX, XXX−XXX

luminescent properties of the complexes can help researchers in tracking real-time drug intracellular transport and distribution in cells and in monitoring the interactions between the drug and the biological target molecule, thus providing an important research tool for revealing the mechanism of action of the anticancer drugs.

In this work, the nitrogen-donor imino-pyridyl ligand (triphenylmethyl)(pyridin-2-ylmethylene)amine was chosen specifically. First, in order to increase the intracellular imaging capability and anticancer activity of half-sandwich metal compounds, we introduced ligands with multiple benzene rings. In general, the greater number of benzene rings of the ligand, the greater the anticancer activity.[28] Another reason we selected these ligands is based on a previous report from the Sadler group. They found that the anticancer activity of iridium complexes increases dramatically with an increase in the number of benzene rings on the Cp ring.[28] In our study, we used a bulky chelating ligand to investigate whether this rule still exists. The third reason we selected the ligands is because aryl-substituted iminopyridine metal complexes exhibited high catalytic activity and high stereoselectivity.[29] Herein a series of half-sandwich Ir^{III} and Ru^{II} complexes of the type $[(\eta^5\text{-}Cp^x)Ir(N^\wedge N)Cl]PF_6$ and $[(\eta^6\text{-arene})Ru(N^\wedge N)Cl]PF_6$, where Cp^x is Cp* (**1**) of a biphenyl derivative (Cp^{xbiph}) (**2**), the arene is benzene (bz) (**3**), *p*-cymene (*p*-cym) (**4**), 3-phenylpropan-1-ol (bz-PA) (**5**), or 4-phenylbutan-1-ol (bz-BA) (**6**), and (triphenylmethyl)(pyridin-2-ylmethylene)amine is the N^N-chelating ligand, were synthesized and characterized (Chart 1).

Chart 1. Organometallic Ir^{III} Cyclopentadienyl $[(\eta^5\text{-}Cp^x)Ir(N^\wedge N)Cl]PF_6$ and Ru^{II} Arene $[(\eta^6\text{-arene})Ru(N^\wedge N)Cl]PF_6$ Complexes Studied in This Work

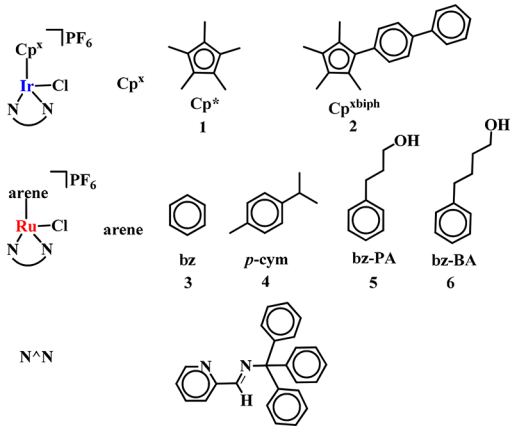

We reported the observation of half-sandwich iridium and ruthenium complexes in living cells by confocal microscopy, which will open a new window to shine light on the mechanism of action of half-sandwich types of metal anticancer complexes. We studied the cancer cell toxicity of these complexes and cellular distribution and uptake with the help of confocal microscopy and ICP-MS. We also investigated their hydrolysis, stability, nucleobase binding, DNA interactions, BSA interactions, catalytic hydride transfer analysis, nuclear morphological changes, cell cycle and cycling, ROS, apoptosis, and mitochondrial membrane potential changes and tried to understand their mechanism of action. The results indicated that these types of metal complexes have a great potential in cancer chemotherapy. The integration of the anticancer potency and the luminescent properties of half-sandwich iridium and ruthenium anticancer complexes offer an opportunity for the construction of novel theranostic platforms.

RESULTS AND DISCUSSION

Syntheses. The dinuclear dichloro-bridged precursor $[(\eta^5\text{-}Cp^*)IrCl_2]_2$ (**dimer 1**) and $[(\eta^5\text{-}Cp^{xbiph})IrCl_2]_2$ (**dimer 2**) were synthesized by microwave-assisted heating of $IrCl_3$ and relative cyclopentadienyl ligand.[30] Dimeric μ-chloro-bridged complexes $[(\eta^6\text{-bz})RuCl_2]_2$ (**dimer 3**), $[(\eta^6\text{-}p\text{-cym})RuCl_2]_2$ (**dimer 4**), $[(\eta^6\text{-bz-PA})RuCl_2]_2$ (**dimer 5**), and $[(\eta^6\text{-bz-BA})RuCl_2]_2$ (**dimer 6**) were formed upon conversion of cyclohexa-1,4-diene, α-terpinene, 3′-(2,5-dihydrophenyl)-propanol, and 4′-(2,5-dihydrophenyl)butanol, respectively, with $RuCl_3$ under reflux in absolute ethanol.[31,32] The N^N-chelating ligand[33] was introduced into the complexes to give increasing hydrophobicity and therefore cellular uptake of the complexes. The six Ir/Ru complexes **1**–**6** were synthesized by reactions between the N^N-chelating ligand (triphenylmethyl)(pyridin-2-ylmethylene)amine and the dinuclear iridium/ruthenium precursors dimers in methanol at ambient temperature (Scheme 1). All complexes were newly synthesized and were fully characterized by NMR and mass spectroscopy, as well as elemental analysis. All complexes were isolated as PF_6^- salts.

X-ray Crystal Structures. Single crystals were obtained from the slow diffusion of hexane into a concentrated solution of $[(\eta^5\text{-}Cp^{xbiph})Ir(N^\wedge N)Cl]PF_6$ (**2**), $[(\eta^6\text{-bz})Ru(N^\wedge N)Cl]PF_6$ (**3**), and $[(\eta^6\text{-}p\text{-cym})Ru(N^\wedge N)Cl]PF_6$ (**4**) in CH_2Cl_2. The three X-ray crystal structures were determined, and their molecular structures are shown in Figure 1. Crystallographic data as well as some selected relevant bond parameters are given in Tables S1 and S2. Each complex adopts the expected pseudo-octahedral "three-legged piano-stool" geometry. The

Scheme 1. Synthesis of the N^N-Chelating Ligand and Respective Half-Sandwich Ir^{III} and Ru^{II} Complexes

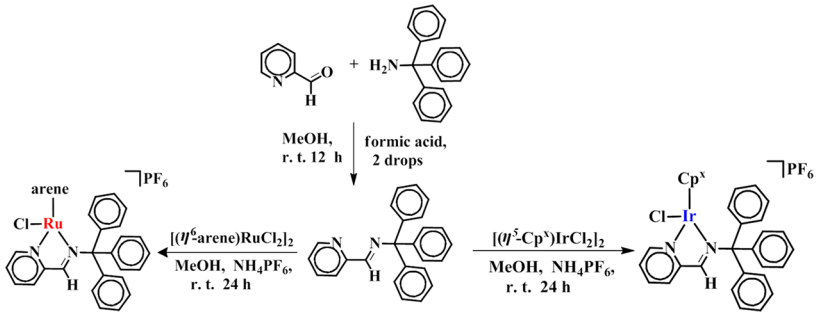

DOI: 10.1021/acs.inorgchem.8b02161
Inorg. Chem. XXXX, XXX, XXX−XXX

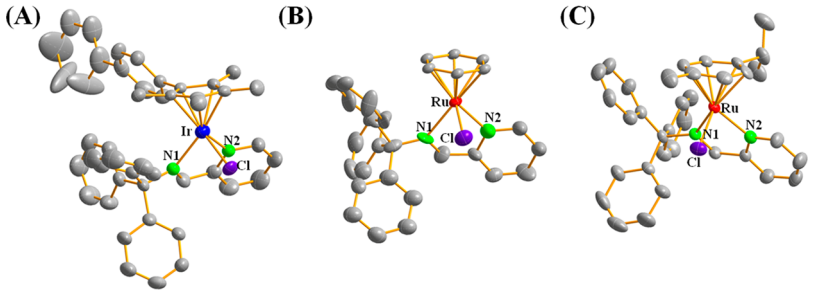

Figure 1. X-ray crystal structures with atom-numbering schemes for (A) $[(\eta^5\text{-Cp}^{xbiph})Ir(N^{\wedge}N)Cl]PF_6$ (**2**), (B) $[(\eta^6\text{-bz})Ru(N^{\wedge}N)Cl]PF_6$ (**3**), and (C) $[(\eta^6\text{-}p\text{-cym})Ru(N^{\wedge}N)Cl]PF_6$ (**4**) with thermal ellipsoids drawn at 50% probability. The hydrogen atoms and PF_6^- counterions have been omitted for clarity.

distance between the iridium center and the centroid of the Cp derivative ring is 1.804 Å, while the distances between the ruthenium center and the centroid of the η^6-arene for complexes **3** and **4** are 1.6826 and 1.7018 Å, respectively. The three complexes have similar metal−Cl and metal−N bond distances. However, slight differences between metal−N_1 and metal−N_2 bond lengths were observed in all three complexes, shown in Table S2. The Ir−N_2 bond length (2.181(4) Å) in complex **2** is significantly longer than that (2.091(5) Å) in the N^N complex $[(\eta^5\text{-Cp*})Ir(bpy)Cl]PF_6$, probably due to the steric hindrance effect of the $(Ph)_3C$ moiety.

Cytotoxicity. The cytotoxic activities of complexes **1**−**6** against HeLa (human cervical cell cancer) and A549 (nonsmall cell lung cancer) cell lines was evaluated. The IC_{50} values (concentration where 50% of the cell growth is inhibited) after 24 h of exposure to complexes **1**−**6** and cisplatin (control) are given in Table 1. Excitingly, all of the six newly synthesized metal complexes displayed medium to potent cell growth inhibitory activity. The iridium Cp* complex **1** showed the highest anticancer activity, ca. 4.2-fold greater than that of cisplatin toward the A549 cell line. In this work, the iridium complexes showed higher anticancer activity in comparison with ruthenium complexes against A549 cells.

Table 1. Inhibition of Growth of A549 and HeLa Cancer Cells by Complexes 1−6 and Comparison with Cisplatin Recorded over a Period of 24 h

	IC_{50} (μM)	
complex	A549	HeLa
$[(\eta^5\text{-Cp*})Ir(N^{\wedge}N)Cl]PF_6$ (**1**)	5.1 ± 0.3	6.5 ± 0.6
$[(\eta^5\text{-Cp}^{xbiph})Ir(N^{\wedge}N)Cl]PF_6$ (**2**)	25.7 ± 2.5	28.7 ± 1.2
$[(\eta^6\text{-bz})Ru(N^{\wedge}N)Cl]PF_6$ (**3**)	29.2 ± 1.6	32.0 ± 1.2
$[(\eta^6\text{-}p\text{-cym})Ru(N^{\wedge}N)Cl]PF_6$ (**4**)	61.3 ± 3.2	54.7 ± 7.4
$[(\eta^6\text{-bz-PA})Ru(N^{\wedge}N)Cl]PF_6$ (**5**)	34.6 ± 2.2	24.1 ± 3.3
$[(\eta^6\text{-bz-BA})Ru(N^{\wedge}N)Cl]PF_6$ (**6**)	77.4 ± 2.4	55.1 ± 1.3
cisplatin	21.3 ± 1.7	7.5 ± 0.2

We investigated the effect of Cp* and its biphenyl substituent of the iridium complexes **1** and **2** and bz, *p*-cymene, 3-phenylpropan-1-ol, and 4-phenylbutan-1-ol substituents of the functionalized ligands of the ruthenium complexes **3**−**6** on cytotoxicity. Complex **1** containing a Cp* ligand exhibited much higher antiproliferative activity in comparison to the Cp^{xbiph} analogue **2**. This result is inconsistent with our previous conclusions which showed that anticancer activity improved significantly with an increase in the number of phenyl rings on the Cp* ring.[16] Sadler and co-workers previously reported that Ir^{III} Cp* complexes $[(\eta^5\text{-Cp*})Ir(phen)Cl]Cl$, $[(\eta^5\text{-Cp*})Ir(bpy)Cl]Cl$, and $[(\eta^5\text{-Cp*})Ir(en)Cl]PF_6$ bearing the N^N-chelating ligands phenanthroline, 2,2′-bipyridine, and ethylenediamine, respectively, were inactive toward A2780 human ovarian cancer cells. This result demonstrates that the N^N-chelating ligand (triphenylmethyl)(pyridin-2-ylmethylene)amine in Cp* Ir complex **1** plays an important role in contributing to the potential anticancer activity. Solubility in aqueous solutions is crucial for the bioavailability of metal-based anticancer drugs. It is still a big challenge to preserve anticancer activity while increasing the water solubility of the drug. In comparison with complex **3**, complex **5** displayed similar anticancer activity against A549 cells; however, complex **5** displayed much better water solubility than **3** by introduction of a propanol group on the benzene ring. The longer pendant (butanol) on the arene ligand in complex **6** led to a decrease in anticancer activity. Iridium complex **1** and ruthenium complex **3** were the two most potent complexes in comparison to their analogues and therefore were chosen to perform all the next experiments to further investigate mechanisms of action. Since the complexes in this work showed more potent toxicity against A549 cells than against HeLa cells, all subsequent experiments were therefore carried out on A549 cells.

Partition Coefficients (log *P*). Cellular uptake levels and cytotoxic potencies of drugs may often be correlated to their lipophilicity. In general, the lipophilicity was consistent with their antiproliferative activity. The log *P* (partition coefficient in oil/water) values for **1**−**6** were determined and ranged from 1.2 to 3.5 (Table 2). The lipophilicity of Ir complexes was higher than that of the Ru complexes.

Hydrolysis and Photophysical Studies. We tested the hydrolysis of complexes **1** and **3** in 67% MeOD/33% D_2O (v/v) using ^1H NMR at 310 K (Figure S1 in the Supporting Information). Deuterated methanol was used to improve the

Table 2. log *P* for Complexes 1−6[a]

	1	2	3	4	5	6
log *P*	3.5 ± 0.6	3.0 ± 0.2	1.7 ± 0.4	1.8 ± 0.7	1.1 ± 0.4	1.2 ± 0.5

[a]The results are the means of three independent experiments.

DOI: 10.1021/acs.inorgchem.8b02161
Inorg. Chem. XXXX, XXX, XXX−XXX

solubility of the complex. The ^{1}H NMR data show that complexes **1** and **3** undergo hydrolysis to the extents of 90% and 13%, respectively (Table 3). The hydrolysis of complexes

Table 3. Hydrolysis Data for Complexes 1 and 3

complex	ligand	metal	extent (%)[a]	k^b (min^{-1})	$t_{1/2}{}^b$ (min)
1	Cp*	Ir	90	0.0084	82.2
3	bz	Ru	13	0.0233	29.8

[a]Monitored by NMR spectra at 310 K. [b]Monitored by UV−vis at 298 K.

1 and **3** in 50% MeOH/50% H_2O (v/v) was monitored by UV−vis at 298 K (Figure S2 in the Supporting Information), and the hydrolysis rate constants and half-lives were determined (Table 3). The half-life values for complexes **1** and **3** were 82.2 and 29.8 min, respectively. Sadler and co-workers reported that hydrolysis that was too rapid ($t_{1/2}$ < 1 min) may lead to the nontoxicity of Ir Cp* complexes.[16] The benzene ring surrounding the nitrogen atom in the chelating ligand may effectively reduce the charge on the nitrogen atom, thereby reducing the rate of hydrolysis.

UV−vis spectra of the imino-pyridyl ligand and complexes **1** and **3** have been acquired in PBS buffer solutions at 298 K (Figure S3 in the Supporting Information). The absorption strength of the ligand is weak in comparison to the complexes. The intense absorption bands of these complexes are in the approximate range 250−500 nm, which could be assigned to mixed charge-transfer modes such as triplet metal to ligand charge transfer (^{1}MLCT and ^{3}MLCT), a mixed ligand-centered transition, and ligand to ligand charge transfer.[34,35]

Interaction with GSH. Tripeptide glutathione (GSH) often coordinates to the metal center of transition-metal complexes and participates in the detoxification of many anticancer metallodrugs. As a result, the stability of complexes **1** and **3** in the presence of GSH was investigated. The reaction between GSH (10 mol equiv) and complex **1** or **3** (1 mM) in 67% MeOD/33% D_2O (v/v) was monitored by NMR spectroscopy at 310 K under an N_2 atmosphere (Figure S4 in the Supporting Information). The peaks corresponding to complex **3** in the NMR spectra decreased after addition of GSH, while new peaks corresponding to GSH adducts of complex **3** increased, indicating that 65% of **3** has reacted with GSH within 2 h. However, complex **1** is much more stable under the same conditions.

Cellular Localization. There is currently a growing interest in the design and development of metallodrugs that target organelles of cancer cells.[36−38] At the beginning, we tested the fluorescence of complexes **1** and **3** (10 μM) using a fluorescence spectrophotometer, where only a weak fluorescence could be detected at λ_{ex} 365 nm. Confocal microscopy is a powerful technique for generating high-resolution images and 3D reconstructions of a specimen with wide application in medicinal and biological research. We then tried to detect images of **1** and **3** in A549 cells. Very excitingly, clear confocal microscopy images were observed for complexes **1** and **3** at λ_{ex} 405 nm. The blue emission by the complexes offered an opportunity to investigate their cellular localization using confocal microscopy images (Figure 2). The images clearly demonstrated that complexes **1** and **3** can effectively penetrate into the A549 cells and that substantial cellular uptake of these complexes occurred within 0.5 h of treatment of A549 cells, suggesting their accretion inside the cells. Interestingly, according to the dual staining of complexes **1** and **3** with the mitochondria staining dye MTDR (MitoTracker Deep Red), a medium Pearson's colocalization coefficient (PCC) of 0.61 in the merged image (overlay, Figure 2A) was obtained for complex **3**, indicating that complex **3** can localize in the mitochondria to a certain extent; however, the intense blue fluorescence in the nucleus (Figure 2A) showed that complex **1** effectively penetrated into nucleus after 30 min incubation. We also probed the specificity of localization of complex **3** with commercial LTDR (Lyso Tracker Deep Red). The confocal images (Figure 2B) indicated that complex **3** is capable of staining lysosome specifically in A549 cells. In comparison with

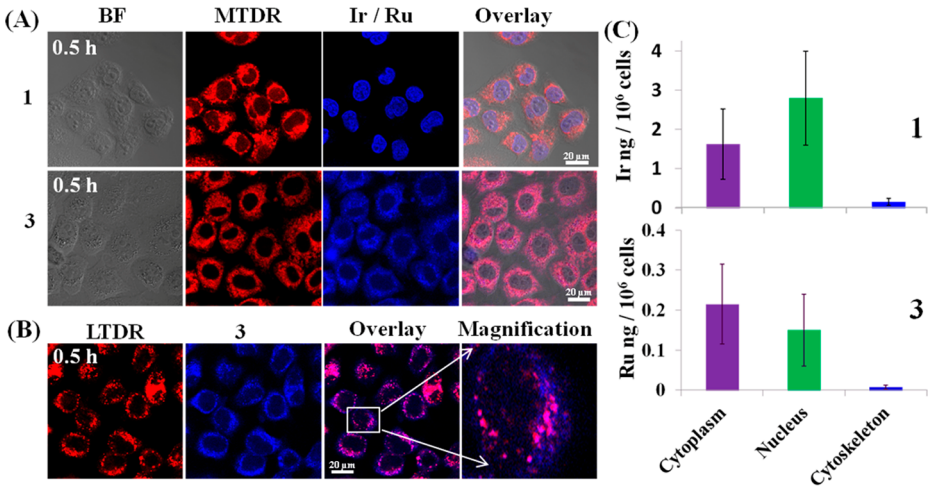

Figure 2. (A) Determination of localization of **1** or **3** with MTDR by confocal microscopy. A549 cells were incubated with **1** or **3** (10 μM, 0.5 h) and then stained with MTDR (100 nM, 0.5 h) at 37 °C. (B) Representative confocal images of A549 cells exposed to **3** with LTDR. A549 cells were incubated with **3** (10 μM, 0.5 h) and then stained with LTDR (100 nM, 0.5 h) at 37 °C. Rxcitation and emission bands: for complexes, λ_{ex} 405 nm, λ_{em} 460 ± 30 nm; for MTDR, λ_{ex} 644 nm, λ_{em} 700 ± 30 nm; for LTDR, λ_{ex} 594 nm, λ_{em} 630 ± 30 nm. Scale bar: 20 μm. (C) Iridium/ruthenium content of the cytoplasm, nucleus and cytoskeleton fractions (Ir/Ru ng/10^6 cells) of A549 cells after 24 h of exposure to 10 μM **1** or **3**. The results are the means of two independent experiments in triplicate and are expressed as means ± SDs.

DOI: 10.1021/acs.inorgchem.8b02161
Inorg. Chem. XXXX, XXX, XXX−XXX

localization with mitochondria, however, less overlap was observed for complex **3** with LTDR with a PCC value of 0.49.

Hoechst33342 and DAPI are two representative examples of small-molecule dyes that have been used as commercial nuclear imaging agents. They intercalate with stacked base pairs and bind to nucleic acids, resulting in a fluorescence enhancement in the nuclear region. Complexes have a certain binding ability to BSA and ctDNA, indicating that the complex has the ability to bind proteins and DNA. Moreover, complex **1** has a strong lipophilicity. The reason that complex **1** selectively stained the nuclei of cells may be related to reaction with histidine or histidine-rich proteins[39] and to intercalation between the stacked base pairs of nucleic acids in the nuclear region.

Complexes **1** and **3** contain the same N^N-chelating ligand and overall charge; however, they displayed totally different specificities of localization in cells, suggesting that the metals and arene/cyclopentadienyl ligands play a key role in the selection of cell organelle localization.

Cellular Uptake. The cellular uptake levels of **1** and **3** in different subcellular compartments were also quantitatively measured by ICP-MS. A549 cells were treated with **1** and **3** for 24 h, and the metal content of the isolated cytoplasm, nucleus, and cytoskeleton fractions from the A549 cells was determined (Figure 2C and Table S3 in the Supporting Information). For complex **1**, the concentration of iridium in the nucleus was around 2 times higher than that in the cytoplasm, while for complex **3**, more ruthenium passed into the cytoplasm than into the nucleus. These results are consistent with the observations of confocal microscopy images.

Then we studied the cellular uptake mechanisms of **1** and **3**. Small molecules can pass through cells through energy-independent (facilitated diffusion and passive diffusion) or energy-dependent (endocytosis and active transport) pathways. As shown in Figure 3, incubation of A549 cells with complexes **1** and **3** at lower temperature (4 °C) or with the treatment of the metabolic inhibitor CCCP (carbonyl cyanide *m*-chlorophenyl hydrazone) results in a significantly reduced cellular uptake efficiency (Figure 3 and Figure S5 in the Supporting Information). Pretreatment of the cells with chloroquine, an endocytosis modulator which can inhibit the acidification of endosomes, gave rise to little effect on the cellular uptake levels of complexes **1** and **3**. The results indicate that complexes **1** and **3** were transported into A549 cells possibly through an energy-dependent pathway and do not rely on endocytic pathways: e.g., via energy-dependent active transport. The two complexes showed similar uptake mechanisms, but higher uptake levels were observed for **1** than for **3**, which suggested that Cp* iridium might be more advantageous for cell penetration than the arene ruthenium moiety.

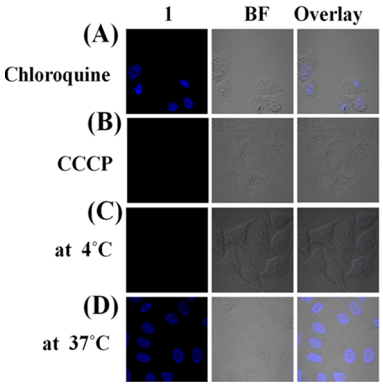

Figure 3. Confocal microscopy images of A549 cells after incubation with **1** under various conditions (λ_{ex} 405 nm, λ_{em} 470 ± 30 nm). (A) Cells were preincubated with chloroquine (50 μM) for 1 h at 37 °C and then incubated with **1** (10 μM) at 37 °C for 60 min. (B) Cells were preincubated with CCCP (50 uM) for 1 h at 37 °C and then incubated with **1** (10 μM) at 37 °C for 60 min. (C) Cells were incubated with **1** (10 μM) at 4 °C for 60 min. (D) Cells were incubated with **1** (10 μM) at 37 °C for 10 min.

Interaction with Nucleobases. As DNA is often an important target for transition-metal-based anticancer drugs, the binding of the model nucleobases 9-ethylguanine (9-EtG) and 9-methyladenine (9-MeA) to complexes **1** and **3** was studied. Nucleobase 9-MeA or 9-EtG (2 mol equiv) was added to a solution of **1** or **3** (1.0 mM) in 67% MeOD/33% D_2O (v/v), and ^{1}H NMR spectra were monitored at different time intervals at 310 K (Figure S6 in the Supporting Information). On the basis of ^{1}H NMR peak integrals, the resulting percentages of nucleobase adduct are given in Table S4 in the Supporting Information. No reaction occurred for complex **1** with the two nucleobases. The ^{1}H NMR data showed that complex **3** bound to 9-ethylguanine (around 23% of **3** reacted) but not 9-MeA. The weak nucleobase binding of these complexes can probably be attributed to the sterically hindered triphenyl group in the chelating ligand.

Interaction with Plasmid DNA. To gain insight into the DNA cleavage ability of these complexes, plasmid pBR322 DNA (10 μM) was incubated with complexes **1** and **3** (0−25 μM) for 3 h and then was monitored using agarose gel electrophoresis in a buffer (40 mM Tris-HCl/1 mM EDTA (disodium salt) at pH 8.3. Previous study has shown that the binding of unwinding agents to the closed circular DNA resulted in a decreased migration rate of DNA in agarose gel.[40] However, no DNA cleavage occurred upon the treatment of these complexes, even at a high concentration of 100 μM (Figure S7 in the Supporting Information).

Interaction with ctDNA. The mitochondria and nucleus accumulation of these complexes as mentioned above prompted us to explore the interaction of these complexes toward calf thymus DNA (ctDNA). UV−vis spectroscopy was employed to investigate the possible binding modes to ctDNA and determine their binding constants (K_b). Complex binding with DNA through intercalation usually leads to hypochromism and bathochromism.[41] Upon the addition of increasing concentrations of ctDNA to the solution of complexes **1** and **3**, a hypochromic effect is observed at 221−224 nm in the UV−vis spectra (Table 4 and Figure S8 in the Supporting Information), which provides evidence for possible intercalative binding to DNA.[42] The hypochromism is as high as 34.8 and 33.4%, respectively, and bands of both complexes **1** and **3**

Table 4. Absorption Spectroscopic Properties of the Ir^{III}/Ru^{II} Complexes on Binding to ctDNA

	absorption λ_{max} (nm)				
complex	free	bound[a]	$\Delta\lambda$	hypochromicity (%)	K_b (10^5 M^{-1})
1	221	224	3	34.8	6.9
3	219	223	4	33.4	1.2

[a][M] = 5 μM at [DNA]/[M] = 72.

DOI: 10.1021/acs.inorgchem.8b02161
Inorg. Chem. XXXX, XXX, XXX−XXX

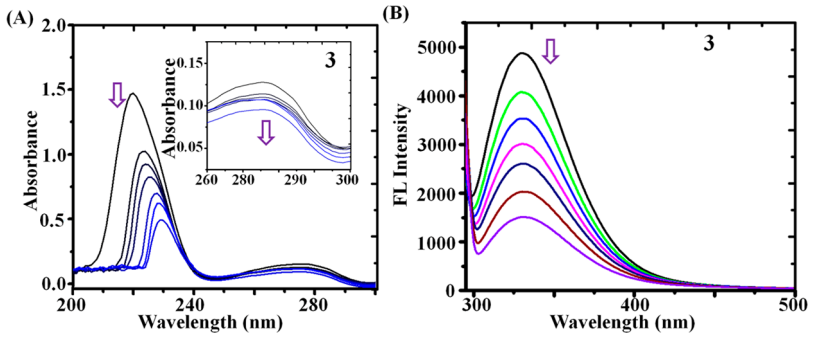

Figure 4. (A) UV−vis spectrum of BSA in 5 mM Tris-HCl/10 mM NaCl buffer solution (pH 7.2) upon addition of complex **3** (0−3.0 μM). The arrows show the direction of changes in absorbance upon increasing the concentration of the complex. (B) Fluorescence spectra of BSA (0.5 μM; λ_{ex} 280 nm; λ_{em} 343 nm) in the absence and presence of complex **3** (0−3.0 μM). The arrow shows the intensity changes with increasing concentration of the Ru(II) complex.

showed red shifts. The binding constants K_b were calculated. The values of the binding constant of the investigated complexes with DNA are similar. Interaction with ctDNA plays an important role in cancer drug design and development. Sheldrick and co-workers reported methyl-substituted polypyridyl ligands of half-sandwich Ru(II) and Rh(III) complexes, which forcefully bond to DNA and regulated apoptosis.[43] Pandey et al. also investigated DNA binding and topoisomerase II inhibitory activity of water-soluble Ru(II) and Rh(III) arene complexes.[44] DNA binding affinity seems to enhance the anticancer activity of Ru(II)-arene complexes.[45]

Study of BSA Interactions. Drug−protein interactions might be crucial for drug transport, release, biodistribution, and toxicity.[46] Serum albumin (SA) is the main protein in blood plasma. Research on anticancer metallodrugs and HSA (human serum albumin) interactions is of great importance in an understanding of drug pharmacokinetics and drug−protein interactions.

The structure of bovine serum albumin (BSA) is similar to that of HSA and is easily obtained. The UV−vis absorption spectra of BSA in the absence and presence of the metal complexes **1** and **3** are shown in Figure 4A and Figures S9 and S10A in the Supporting Information. Upon addition of the complexes, the absorption peaks shifted toward longer wavelength and dramatically decreased at 218 nm. The decrease is due to the induced perturbation of the α-helix of BSA by the complexes.[47] The red shift of the absorption spectra can be attributed to the effect of the polar solvent (water).[48] With addition of metal complexes to BSA, there was no shift but a progressive decrease in the absorption peak of BSA at 278 nm was observed for complexes **1** and **3**. The changes suggest that these two complexes can interact with BSA molecules and the microenvironment of the three aromatic acid residues in BSA (Trp, Tyr, and Phe) was altered upon addition of metal complexes.[49]

Fluorescence quenching studies were further performed to investigate the binding ability of the metal complexes with BSA in Figure 4B and Figure S10B in the Supporting Information. The decrease in fluorescence of BSA is a consequence of the reduced excitation power due to the increasing concentration of the added complexes. Static quenching, which usually causes perturbation of the absorption spectrum of the fluorophore,[50] are operative in this system. The values of K_{sv}, K_b, and n for all four complexes are shown in Table 5 and Figure S11 in the Supporting Information.

Table 5. Values of K_{sv}, K_b, and n for Complexes 1 and 3 at 298 K

complex	K_{sv} (10^6 M^{-1})	K_b (10^5 M^{-1})	n
1	1.28 ± 0.37	3.3	2.1
3	1.02 ± 0.18	4.3	0.6

A plot of the double log graph of the fluorescence data was shown in Figure S12 in the Supporting Information. The magnitudes of K_b and K_{sv} of the two complexes are 10^5 and 10^6 M^{-1}, respectively, indicating moderate binding abilities to BSA. The Cp* Ir complex **1** showed a larger number of the binding sites with an n value of 2.1, indicating about two binding sites in BSA for **1**.

The effect of **1** and **3** on BSA synchronous fluorescence spectroscopy is shown in Figure S13 in the Supporting Information. From these results it is concluded that the test compounds affect the tryptophan microenvironment significantly but do not affect the microenvironment of tyrosine residues during the binding process.[51]

Catalytic Oxidation of NADH. To a great extent, the NADH/NAD^+ couple play significant roles as the cofactor in numerous enzymatic reactions. Recently, Sadler and co-workers have reported that Ir^{III} and Ru^{II} cyclopentadienyl complexes can catalytically convert the coenzyme NAD^+/NADH couple through transfer hydrogenation reactions and can produce ROS H_2O_2, thus providing an effective pathway to an oxidant mechanism of action.[52−54] Therefore, reactions between metal complexes **1** and **3** and NADH were investigated. First, the reaction was monitored by ^{1}H NMR in 50% DMSO-d_6/50% D_2O (v/v) at 310 K. Because of the low aqueous solubility of the tested compounds, DMSO-d_6 was conducted to improve the solubility of metal complexes in solution. When NADH (3.5 mol equiv) was added to a 2 mM solution of complex **1**, after 15 min, a sharp singlet at −11.87 ppm was observed in the ^{1}H NMR spectrum which corresponds to the hydride Ir−H (Figure S13 in the Supporting Information). Additionally new peaks at 8.968, 9.347, and 9.528 ppm assignable to the hydrogen atoms at the C4, C6, and C2 positions of the nicotinamide ring of NAD^+ were observed, which indicates that NADH was converted into its oxidized form NAD^+. The large downfield shift of this peak in comparison to that (−8.74 ppm) for $[(\eta^5\text{-Cp*})\text{Ir}(\text{N}\text{^}\text{N})(\text{H})]^+$ (N^N = 2,6-diisopropyl-*N*-(pyridin-2-ylmethylene)-aniline) is notable.[14] Second, to evaluate the real catalytic activity, we incubated 100 μM NADH in a solution of 50%

DOI: 10.1021/acs.inorgchem.8b02161
Inorg. Chem. XXXX, XXX, XXX−XXX

MeOH/50% H_2O (v/v) as a control (Figure S14A in the Supporting Information). The catalytic ability of complexes **1** and **3** (ca. 1 μM) with NADH (100 μM) in 50% MeOH/50% H_2O (v/v) was monitored by UV−vis at 298 K (Figure S14B,C in the Supporting Information). The conversion of NADH to NAD^+ can be simply measured by the UV absorption difference at 339 nm, as NADH has a UV absorption at 339 nm while NAD^+ does not. The turnover numbers (TONs) of complexes **1** (18.5) and **3** (12.2) were calculated (Figure S14D in the Supporting Information). The good catalytic behavior of converting NADH to NAD^+ may provide an effective pathway to induce ROS and improve the cytotoxic activity.[53]

Apoptosis Assay. Apoptosis is a process of programmed cell death. Many complexes exert their cytotoxic activity in tumor cells by inducing apoptosis. In order to gain insight into whether the reduction in cell viability is arising from apoptosis, A549 lung cancer cells were treated with complexes **1** and **3** at 0.5, 1, and 2 equipotent concentrations of IC_{50} for 24 h and tested by flow cytometry. As shown in Figure 5 and Table S6

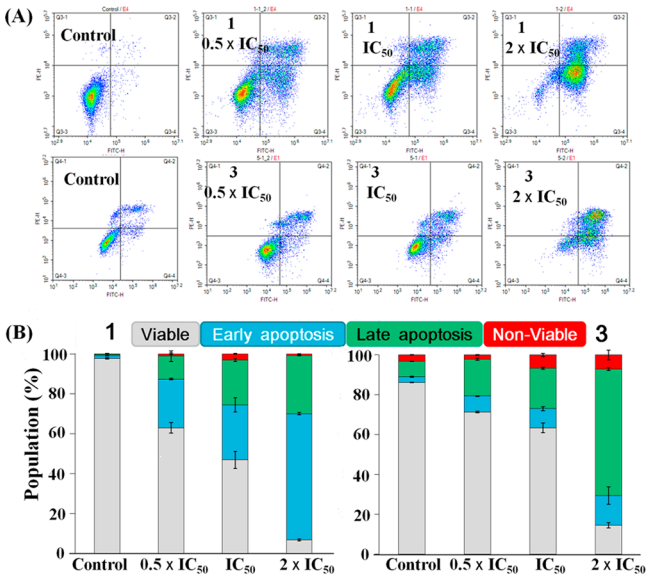

Figure 5. Apoptosis analysis of A549 cells after 24 h of exposure to complexes **1** and **3**, at 310 K determined by flow cytometry using annexin V vs PI staining: (A) populations for cells treated by **1** and **3**; (B) histogram for A549 cells treated with different concentrations of metal complexes **1** and **3** for 24 h.

in the Supporting Information, complex **1** at a concentration of 0.5 × IC_{50} led to 24.5% and 11.5% of A549 cells in early apoptotic and late apoptotic phases after 24 h, respectively. With an increase in the concentrations of metal complexes, a greater population of cells was in apoptosis. Finally, a 92.5% total proportion of early apoptotic and late apoptotic cells were undergoing apoptosis at 2 × IC_{50} of complex **1**, whereas untreated cells remained 97.8% viable. For complex **3**, 78.3% A549 cells were in apoptotic phase at a concentration of 2 × IC_{50}.

To verify whether induction of apoptosis is the major pathway for cytotoxicity of **1** and **3** toward A549 cells, we evaluated the cytotoxicity in the presence of different inhibitors. The cells were treated with necroptosis inhibitor necrostatin-1 (Nec-1), autophagy inhibitor 3-methyladenine (3-MA), the protein synthesis inhibitor cycloheximide (CHX), and the protease inhibitor leupeptin (LPT) (Table S5 in the Supporting Information. The data showed that the cytotoxic effects of **1** and **3** did not change significantly, suggesting that these inhibitors are not operative and apoptosis is the main way to cause cytotoxicity.

Nuclear Morphological Changes. The confocal microscopy technique was employed to gain more insights into the intracellular effects of complex **1** on cell morphological changes during the course of apoptosis. After incubation of A549 cells with complex **1** (10 μM) for the indicated times (1, 5, 24 h) at 37 °C (Figure 6), irregular nuclear morphology, nuclear

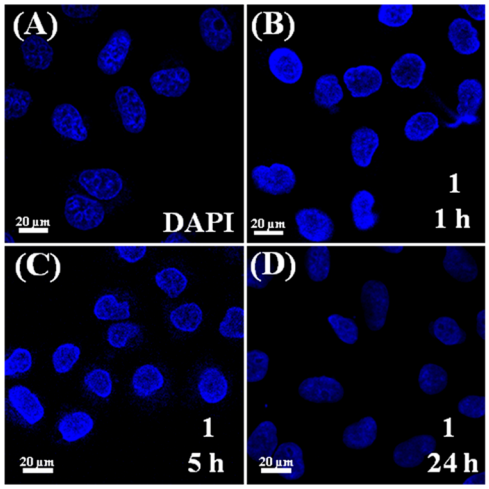

Figure 6. Confocal microscopy images of nuclear condensation in DAPI labeled or complex **1** treated A549 cells for the indicated times at 37 °C. (A) DAPI (1 ng/mL) staining of the nuclei of A549 cells after 1 h. Images of complex **1** (10 μM) (B) after 1 h, (C) after 5 h, and (D) after 24 h. For DAPI and complex **1**: λ_{ex} 405 nm, λ_{em} 460 ± 30 nm. Scale bar: 20 μm.

fragmentation, and chromatin condensation of the nucleus were observed. Control cells were uniformly stained with DAPI and presented round homogeneous nuclei. These results indicated that complex **1** could effectively change nuclear morphology and finally induce A549 cell apoptosis.

Mitochondrial Membrane Potential ($\Delta\psi_m$) Changes. Impairment of mitochondrial functions plays a significant role in both extrinsic and intrinsic apoptosis, such as loss of mitochondrial membrane potential (MMP). The effects of complexes **1** and **3** (at concentrations of 0.25, 0.5, 1, and 2 × IC_{50}) on the MMP of A549 cancer cells was monitored by detecting the red/green fluorescence of JC-1 by flow cytometry (Figure 7 and Table S7 in the Supporting Information). JC-1 can be aggregated in a MMP-dependent manner in mitochondria, where green fluorescence indicates a decrease in MMP and red fluorescence means high membrane potentials. When cells were treated with complexes **1** and **3**, an increasing portion of cells lost their MMP. The two complexes caused a marked decrease in MMP, as evidenced by the fluorescence shift from red to green. After 24 h treatment, the percentage of cells with mitochondrial membrane depolarization increased from 6.9% to 82.0% and 62.0%, respectively, for **1** and **3**. A decrease in MMP is an early manifestation of apoptosis. Once the mitochondrial membrane potential is lost, the cells enter an irreversible phase of apoptosis. As a result, these complexes may induce cancer cell death through the dysfunction of the mitochondrial membrane

DOI: 10.1021/acs.inorgchem.8b02161
Inorg. Chem. XXXX, XXX, XXX−XXX

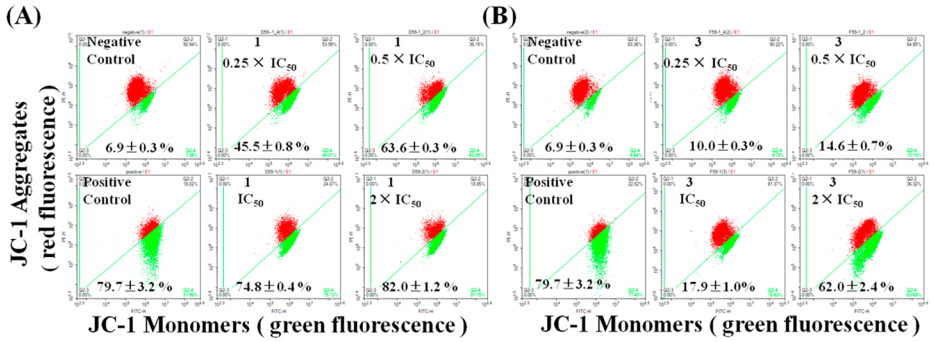

Figure 7. Effects of (A) complex **1** and (B) complex **3** on MMP analyzed by JC-1 staining and flow cytometry. A549 cells were treated with vehicle or complexes at the indicated concentrations for 24 h.

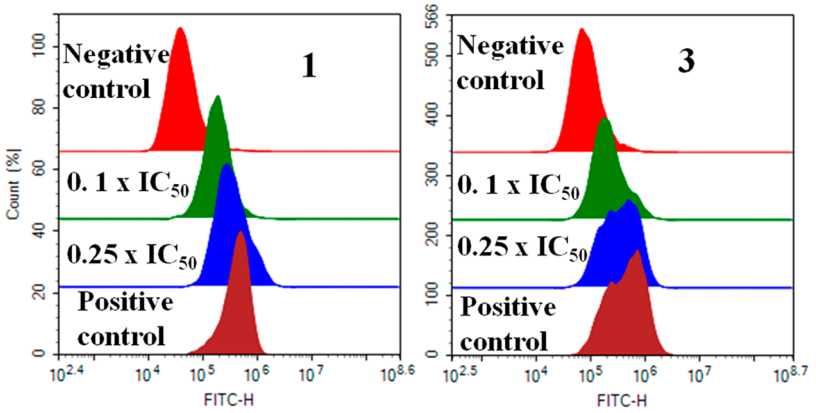

Figure 8. Flow cytometry analysis on ROS induction in A549 cancer cells treated with complexes **1** and **3** at the indicated concentrations for 24 h.

potential. Complex **1** can penetrate the cell membrane, enter cells, and target the nucleus. The nucleus is the largest organelle in the cell and is also the control center of all activities in the cell. It can regulate the function of mitochondria, such as the mitochondrial membrane permeability and cytochrome *c* release. To explore the relationship between cytotoxicity and mitochondrial membrane potential, cyclosporine A (CsA, a desensitizer of mitochondrial permeability transition pore) was used (Figure S16 and Table S5 in the Supporting Information. The cell cytotoxicity of complex **1** was decreased in the presence of CsA, indicating that a decrease in MMP can increase cytotoxicity.

Induction of Intracellular Reactive Oxygen Species (ROS). Reactive oxygen species are very important in regulating cell proliferation, death, and signaling. The excessive generation of ROS is usually an important MoA of anticancer agents.[53] The ROS generated in cancer cells were detected using the fluorescent probe DCFH-DA, which could easily be hydrolyzed and penetrate the cell membrane to form DCFH. DCFH has no fluorescence and cannot pass through the cell membrane. Since ROS produced in cells could oxidize DCFH into fluorescent DCF, thus the fluorescence intensity of DCF can indicate the level of intracellular ROS. To investigate the efficacy of complexes **1** and **3** for inducing ROS generation, the ROS levels in A549 cancer cells induced by the two complexes at the indicated concentrations for 24 h were detected by flow cytometry analysis (Figure 8 and Figure S17 in the Supporting Information). The ROS level is represented by the relative fluorescence intensity (percent of control). When A549 cancer cells were exposed to **1** and **3** for 24 h, significant increases of ROS levels in cancer cells were observed. The level of ROS induced by **1** and **3** was obviously elevated in a dose-dependent manner. It has been reported that complexes can catalytic hydride transfer from NADH to oxygen to produce the ROS H_2O_2 as a product.[50] Therefore, we tested whether H_2O_2 is produced in the cells. The experimental results show that the content of H_2O_2 in **1** and **3** treated A549 cancer cells obviously increased at 0.25 × IC_{50} (Figure S17 in the Supporting Information).

It has already been reported that the ability of drugs to induce apoptosis in cancer cells depends upon the ability to generate ROS.[55] To probe the effects of ROS generated by **1** and **3** on the induced apoptosis and cytotoxicity, A549 cancer cells were pretreated with the ROS scavenger NAC (*N*-acetyl-L-cysteine) before the addition of **1** or **3**. The higher cell viability and lower cytotoxicity in NAC-treated cells indicated that the presence of NAC obviously protected the cells from the attack of **1** and **3** (Figure S18 and Tables S8 and S9 in the Supporting Information), thus showing the critical function of ROS in the induced apoptosis and cytotoxicity of **1** and **3**. From the available data, it was inferred that cells treated with the complexes efficiently increase ROS generation in A549 cells and consequently induce apoptosis and cytotoxicity. The increases in ROS levels may provide a pathway to kill cancer cells.

Cell Cycle Analysis. Next we investigated whether the cell cycle arrest was the result of inhibition of cancer cell proliferation. The cell cycle progression of A549 cancer cells after exposure with 2 × IC_{50} of complexes **1** and **3** for 24 h was analyzed by flow cytometry (Figure 9 and Table S10 in the Supporting Information). Upon exposure of the cells to complex **3**, the percentage of cells in the G_0/G_1 phase of the

DOI: 10.1021/acs.inorgchem.8b02161
Inorg. Chem. XXXX, XXX, XXX−XXX

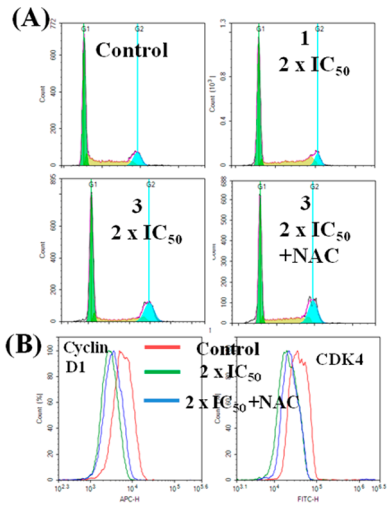

Figure 9. Cell cycle analysis of A549 cancer cells after 24 h of exposure to complexes **1** and **3** at 2 × IC_{50} and pretreatment with the general ROS scavenger NAC before exposure to complexes **1** or **3**. Cell staining for flow cytometry was carried out using PI. (A) Cell populations in each cell cycle phase were determined for control and complexes **1** and **3** at 2 × IC_{50} and cell pretreatment with 10 mM NAC for 1 h and then treatment with complex **3** for 24 h. (B) The changes in CDK 4/cyclin D1 level on exposure to complex **3** for 24 h waswere measured by flow cytometry.

cell cycle increased to 10.4%, indicating that the complex arrested the cell cycle at the G_0/G_1 phase; however, no significant changes were observed for complex **1**. As cells prepare for DNA synthesis in the G_0/G_1 phase, complex **3** could probably prevent RNA synthesis to an extent by interacting with nucleic acid base.

In order to investigate in what way the cycles are altered, we examined the changes of cyclin after drug exposure. CDK 4 (cyclin-dependent kinase 4) is essential in the progression of the G_0/G_1 phase by forming CDK 4-cyclin D1 complexes.[56] Inactivation of CDK 4/cyclin D1 is related to the G_0/G_1 phase arrest. As shown in Figure 9B, a decrease in accumulation of CDK 4 and cyclin D1 was detected, suggesting that complex **3** induced G_0/G_1 phase arrest by inactivation of CDK 4 and cyclin D1.

We further investigated whether the changes in the cell cycle correlate with ROS. We performed the cell cycle assay in the presence of NAC. In comparison with the cell cycle result without NAC, a negligible decrease in the proportion of the G_0/G_1 phase was observed for cells pretreated with NAC, and the changes in CDK 4/cyclin D1 level were also not obvious. Therefore, ROS may not contribute to the changes in cell cycle. For complex **1**, the cell cycle arrest is not the main cause of inhibition of cancer cell proliferation; it caused cell apoptosis mainly via an ROS-dependent mitochondrial pathway. However, these cell cycle disturbances may contribute to the apoptosis induced by complex **3**.

CONCLUSION

In conclusion, this work has demonstrated the ready intracellular observation of half-sandwich iridium and ruthenium anticancer complexes using confocal microscopy. Confocal microscopy provides insights into the microscopic mechanisms including cellular uptake, distribution, and interaction with biological targets, which are difficult to obtain with other techniques.

A systematic study on the anticancer behavior of half-sandwich Ir^{III} and Ru^{II} complexes $[(\eta^5\text{-}Cp^x)Ir(N^\wedge N)Cl]PF_6$ and $[(\eta^6\text{-arene})Ru(N^\wedge N)Cl]PF_6$ was performed. These efforts revealed that this class of compounds as potential anticancer drugs exhibited potent in vitro anticancer activity. Ir Cp* complex **1** was discovered as a new lead candidate, as it is more potent than the established metal-based anticancer drug cisplatin. Herein, we have studied the substituent effects of the cyclopentadienyl and arene ligands and the metal center effect on their chemical (hydrolysis, nucleobase binding, GSH reactions) and anticancer activity. Excitingly, Ir complex **1** and Ru complex **3** are trackable in cells by confocal microscopy, which has been employed to determine biodistribution in cells and will facilitate future in vivo studies. We showed that subtle structural changes can have a large influence on both the cytotoxicity and cellular localization. Complex **1** was shown to accumulate in nuclei; however, **3** was mainly located in mitochondria by using confocal microscopy and ICP-MS. The two complexes entered the cancer cells mainly through energy-dependent active transport. These Ir^{III}/Ru^{II} complexes showed similar binding affinities to ctDNA and BSA. The fluorescence quenching of BSA by the metal complexes is due to static quenching. These types of complexes are effective catalysts for oxidation of NADH to NAD^+ by robbing hydride from NADH with the formation of detectable Ir−H species, which may induce ROS in cancer cells. Indeed, complexes **1** and **3** increased ROS levels significantly in A549 cells even at the indicated concentrations after 24 h of drug exposure, which resulted in the majority of cancer cells being influenced by the generation of ROS. Complexes **1** and **3** caused a marked decrease in MMP. Loss of mitochondrial membrane potential (MMP) and excessive generation of ROS play significant roles in intrinsic apoptosis. In addition, complex **3** inactivated CDK 4/cyclin D1 and arrested the cell cycle at the G_0/G_1 phase. Moreover, obvious apoptosis was induced when A549 cancer cells were treated with different IC_{50} concentrations of complexes **1** and **3**. This work paves the way to track and monitor half-sandwich metal complexes in cells, shines a light on understanding their mechanism of actions, and indicates the potential application of half-sandwich metal complexes as theranostic agents.

EXPERIMENTAL SCETION

Materials. The reagents $IrCl_3 \cdot nH_2O$ (≥99% purity), hydrated $RuCl_3 \cdot nH_2O$ (≥99% purity), 2,3,4,5-tetramethyl-2-cyclopentenone (95%), 1,2,3,4,5-pentamethyl-cyclopentadiene (95%), butyllithium solution (1.6 M in hexane), cyclohexa-1,4-diene, 4-phenylbutan-1-ol, 3-phenylpropan-1-ol, α-terpinene, picolinaldehyde, and triphenylmethanamine were purchased from Sigma-Aldrich. NH_4PF_6 (Alfa Aesar), cisplatin (Sigma-Aldrich), MTDR (Life Technologies), LTDR (Life Technologies), MTT (3-(4,5-dimethylthiazol-2-yl)-2,5-diphenyltetrazolium bromide, Sigma-Aldrich), *N*-acetyl-L-cysteine (Sigma-Aldrich), Annexin V-FITC Apoptosis Detection Kit (Sigma-Aldrich), hydrogen peroxide assay kit (Beyotime, Jiangshu, China), Cyclin D1 Rabbit mAb (Cell Signaling), Goat anti-Rabbit lgG H&L (abcam), Anti-Cdk4 antibody [EPR4513-32-7] (abcam), JC-1 (Sigma-Aldrich), PBS (Sangon Biotech), Pand I (Sigma-Aldrich) were all used as received. $Cp^{xbiph}H$[30] was prepared as described. For the biological experiments, BSA, Supercoiled pBR322 DNA, and 6X loading buffer (0.05% bromophenol blue, 0.035% xylene cyanol FF, 36% glycerol, and 30 mM EDTA) were purchased from TaKaRa Biotechnology (Dalian, China). Calf thymus DNA (ctDNA), Tris, and DMEM medium were obtained from Sigma-Aldrich. Testing compounds was dissolved in DMSO and diluted with the tissue culture medium before use. During

DOI: 10.1021/acs.inorgchem.8b02161
Inorg. Chem. XXXX, XXX, XXX−XXX

the cell experiment, the DMSO concentration was maintained at 1% (v/v).

Syntheses. The ^{1}H NMR (500 MHz) spectra of the ligand (triphenylmethyl)(pyridin-2-ylmethylene)amine and complexes **1**−**6** are shown in Figures S19−S25.

Synthesis of the Ligand. The ligand (triphenylmethyl)(pyridin-2-ylmethylene)amine was synthesized according to a reported procedure.[33] A solution of picolinaldehyde (5 mM), triphenylmethanamine (5 mM), and a catalytic amount of formic acid in methanol (15 mL) was stirred at room temperature for 12 h. The solvent was evaporated to dryness on a rotary evaporator, and a crude product was obtained, which was washed with water (5 mL) and dried over anhydrous alumina at room temperature. The products were obtained as a white powder. ^{1}H NMR (500 MHz, DMSO): δ 8.60 (d, J = 4.1 Hz, 1H), 8.34−8.31 (m, 1H), 7.97 (td, J = 7.7, 1.6 Hz, 1H), 7.77 (s, 1H), 7.51 (ddd, J = 7.5, 4.8, 1.2 Hz, 1H), 7.37 (t, J = 7.4 Hz, 6H), 7.33−7.28 (m, 3H), 7.22 (dd, J = 5.3, 3.2 Hz, 6H).

Synthesis of Complexes 1−6: General Method. The ligand (triphenylmethyl)(pyridin-2-ylmethylene)amine (0.10 mM) and metal dimer $[(\eta^5\text{-Cp}^x)\text{IrCl}_2]_2$ or $[(\eta^6\text{-arene})\text{RuCl}_2]_2$ (0.05 mM) were dissolved in methanol in a dry round-bottom flask equipped with a stirrer and placed under a nitrogen atmosphere. After constant stirring for 4 h, NH_4PF_6 (0.2 mM) was added at room temperature. The reaction mixture was stirred for 20 h at room temperature, and the progress o the f reaction was monitored by TLC. After complete conversion, methanol was removed under reduced pressure and the product was dissolved in dichloromethane, filtered through a Celite filtration funnel, and recrystallized by slow diffusion of *n*-hexane in a concentrated solution of the compound in dichloromethane to obtain the corresponding complexes **1**−**6**.

*$[(\eta^5\text{-Cp*})\text{Ir(N^N)Cl}]\text{PF}_6$ (**1**).* Yield: 52.48 mg, 61.3%. ^{1}H NMR (500 MHz, DMSO): δ 8.61 (d, J = 4.7 Hz, 1H), 8.33 (d, J = 7.9 Hz, 1H), 7.98 (t, J = 7.0 Hz, 1H), 7.77 (s, 1H), 7.51 (ddd, J = 7.5, 4.8, 1.1 Hz, 1H), 7.37 (t, J = 7.5 Hz, 6H), 7.31 (t, J = 7.3 Hz, 3H), 7.24−7.21 (m, 6H), 1.75 (s, 15H). Anal. Calcd For $[(\eta^5\text{-Cp*})\text{Ir(N^N)Cl}]\text{PF}_6$ (856.3): C, 49.09; H, 4.12; N, 3.27. Found: C, 49.20; H, 4.02; N, 3.23. MS: m/z 711.34 $[(\eta^5\text{-Cp*})\text{Ir(N^N)Cl}]^+$.

*$[(\eta^5\text{-Cp}^{\text{xbiph}})\text{Ir(N^N)Cl}]\text{PF}_6$ (**2**).* Yield: 40.05 mg, 40.3%. ^{1}H NMR (500 MHz, DMSO): δ 13.59 (d, J = 9.6 Hz, 2H), 9.54 (d, J = 9.7 Hz, 3H), 8.80 (d, J = 5.4 Hz, 2H), 8.57−8.13 (m, 5H), 8.05−7.65 (m, 8H), 7.64−7.23 (m, 8H), 1.83 (dd, J = 33.5, 10.8 Hz, 12H). Anal. Calcd For $[(\eta^5\text{- Cp}^{\text{xbiph}})\text{Ir(N^N) Cl}]\text{PF}_6$ (994.47): C, 55.56; H, 4.16; N, 2.82. Found: C, 55.22; H, 4.32; N, 2.73. MS: m/z 849.7 $[(\eta^5\text{-Cp}^{\text{xbiph}})\text{Ir(N^N)Cl}]^+$.

*$[(\eta^6\text{-bz})\text{Ru(N^N)Cl}]\text{PF}_6$ (**3**).* Yield: 45.43 mg, 61.3%. ^{1}H NMR (500 MHz, DMSO): δ 9.63 (d, J = 5.3 Hz, 1H), 8.78 (s, 1H), 8.32 (d, J = 7.9 Hz, 1H), 8.26 (t, J = 8.2 Hz, 1H), 7.89−7.86 (m, 1H), 7.45 (ddd, J = 27.3, 19.4, 7.3 Hz, 15H), 5.61 (s, 6H). Anal. Calcd For $[(\eta^6\text{-bz})\text{Ir(N^N)Cl}]\text{PF}_6$ (708.04): C, 52.59; H, 3.70; N, 3.96. Found: C, 52.30; H, 3.62; N, 3.86. MS: m/z 527.93 $[(\eta^6\text{- bz})\text{Ir(N^N)}]^+$.

*$[(\eta^6\text{-p-cym})\text{Ru(N^N)Cl}]\text{PF}_6$ (**4**).* Yield: 55.31 mg, 72.4%. ^{1}H NMR (500 MHz, $CDCl_3$): δ 9.48 (s, 1H), 8.37 (s, 2H), 8.06 (s, 2H), 7.84 (d, J = 61.2 Hz, 3H), 7.47 (dd, J = 46.9, 7.3 Hz, 12H), 5.83 (s, 1H), 5.27 (s, 1H), 4.71 (s, 1H), 4.48 (s, 1H), 2.43 (s, 1H), 2.17 (s, 3H), 1.00−0.76 (m, 6H). Anal. Calcd For $[(\eta^6\text{-p-cym})\text{Ir(N^N)Cl}]\text{PF}_6$ (764.15): C, 55.01; H, 4.48; N, 3.67. Found: C, 55.20; H, 4.52; N, 3.76. MS: m/z 584.75$[(\eta^6\text{-p-cym})\text{Ir(N^N)} + \text{H}]^+$.

*$[(\eta^6\text{-bz-PA})\text{Ru(N^N)Cl}]\text{PF}_6$ (**5**).* Yield: 53.51 mg, 69.8%. ^{1}H NMR (500 MHz, DMSO): δ 9.57 (d, J = 5.3 Hz, 1H), 8.76 (s, 1H), 8.35−8.21 (m, 3H), 7.92−7.81 (m, 2H), 7.45 (ddd, J = 26.9, 15.6, 7.3 Hz, 13H), 5.71 (t, J = 6.0 Hz, 1H), 5.66 (d, J = 6.3 Hz, 1H), 5.38 (t, J = 5.6 Hz, 1H), 5.03−4.96 (m, 2H), 4.55 (t, J = 5.0 Hz, 1H), 2.45−2.38 (m, 2H), 1.65 (ddd, J = 12.9, 8.8, 5.4 Hz, 2H), 1.53 (ddd, J = 13.5, 11.1, 6.7 Hz, 2H). Anal. Calcd For $[(\eta^6\text{-bz-PA})\text{Ir(N^N)Cl}]\text{PF}_6$ (766.12): C, 53.30; H, 4.21; N, 3.66. Found: C, 53.25; H, 4.32; N, 3.79. MS: m/z 586.72 $[(\eta^6\text{-bz-PA})\text{Ir(N^N)} + \text{H}]^+$.

*$[(\eta^6\text{-bz-BA})\text{Ru(N^N)Cl}]\text{PF}_6$ (**6**).* Yield: 50.72 mg, 65.0%. ^{1}H NMR (500 MHz, DMSO): δ 9.56 (d, J = 5.4 Hz, 1H), 8.76 (s, 1H), 8.31 (d, J = 6.5 Hz, 1H), 8.26 (t, J = 7.7 Hz, 1H), 7.88 (t, J = 5.8 Hz, 1H), 7.45 (ddd, J = 26.8, 14.7, 7.3 Hz, 13H), 5.73 (dd, J = 13.6, 7.7 Hz, 2H), 5.64 (d, J = 5.9 Hz, 1H), 5.40 (t, J = 5.6 Hz, 1H), 5.02 (t, J = 6.0 Hz, 1H), 4.96 (d, J = 6.5 Hz, 1H), 2.38−2.29 (m, 2H), 1.64−1.27 (m, 6H). Anal. Calcd For $[(\eta^6\text{-bz-BA})\text{Ir(N^N)Cl}]\text{PF}_6$ (780.14): C, 53.88; H, 4.39; N, 3.59. Found: C, 53.72; H, 4.42; N, 3.79. MS: m/z 600.35 $[(\eta^6\text{-bz-BA})\text{Ir(N^N)} + \text{H}]^+$.

■ ASSOCIATED CONTENT

Ⓢ Supporting Information

The Supporting Information is available free of charge on the ACS Publications website at DOI: 10.1021/acs.inorgchem.8b02161.

Experimental details and figures and tables as described in the text (PDF)

Accession Codes

CCDC 1819246−1819248 contain the supplementary crystallographic data for this paper. These data can be obtained free of charge via www.ccdc.cam.ac.uk/data_request/cif, or by emailing data_request@ccdc.cam.ac.uk, or by contacting The Cambridge Crystallographic Data Centre, 12 Union Road, Cambridge CB2 1EZ, UK; fax: +44 1223 336033.

■ AUTHOR INFORMATION

Corresponding Author

*E-mail for Z.L.: liuzheqd@163.com.

ORCID

Lihua Guo: 0000-0002-0842-9958

Zhe Liu: 0000-0001-5796-4335

Notes

The authors declare no competing financial interest.

■ ACKNOWLEDGMENTS

We thank the National Natural Science Foundation of China (Grant No. 21671118) and the Taishan Scholars Program for support.

■ REFERENCES

(1) Wang, X.; Wang, X.; Guo, Z. Functionalization of Platinum Complexes for Biomedical Applications. *Acc. Chem. Res.* **2015**, *48*, 2622−2631.

(2) Johnstone, T. C.; Suntharalingam, K.; Lippard, S. J. The Next Generation of Platinum Drugs: Targeted Pt(II) Agents, Nanoparticle Delivery, and Pt(IV) Prodrugs. *Chem. Rev.* **2016**, *116*, 3436−3486.

(3) Han, Y.; Tian, Z.; Zhang, S.; Liu, X.; Li, J.; Li, Y.; Liu, Yi.; Gao, M.; Liu, Z. Half-sandwich IridiumIII N-heterocyclic Carbene Antitumor Complexes and Biological Applications. *J. Inorg. Biochem.* **2018**, *189*, 163−171.

(4) Leung, C. H.; Zhong, H. J.; Chan, D. S.H.; Ma, D. L. Bioactive iridium and rhodium complexes as therapeutic agents. *Coord. Chem. Rev.* **2013**, *257*, 1764−1776.

(5) Albada, B.; Metzler-Nolte, N. Organometallic−Peptide Bioconjugates: Synthetic Strategies and Medicinal Applications. *Chem. Rev.* **2016**, *116*, 11797−11839.

(6) Allardyce, C. S.; Dyson, P. J. Metal-based drugs that break the rules. *Dalton Trans.* **2016**, *45*, 3201−3209.

(7) Needham, R. J.; Sanchez-Cano, C.; Zhang, X.; Romero-Canelón, I.; Habtemariam, A.; Cooper, M. S.; Meszaros, L.; Clarkson, G. J.; Blower, P. J.; Sadler, P. J. In-Cell Activation of Organo-Osmium (II) Anticancer Complexes. *Angew. Chem., Int. Ed.* **2017**, *56*, 1017−1020.

(8) Busto, N.; Valladolid, J.; Martínez-Alonso, M.; Lozano, H. J.; Jalón, F. A.; Manzano, B. R.; Rodríguez, A. M.; Carrión, M. C.; Biver, T.; Leal, J. M.; Espino, G.; García, B. Anticancer Activity and DNA Binding of a Bifunctional Ru(II) Arene Aqua-Complex with the 2,4-Diamino-6-(2-pyridyl)-1,3,5-triazine Ligand. *Inorg. Chem.* **2013**, *52*, 9962−9974.

DOI: 10.1021/acs.inorgchem.8b02161
Inorg. Chem. XXXX, XXX, XXX−XXX

(9) Busto, N.; Valladolid, J.; Aliende, C.; Jalon, F. A.; Manzano, B. R.; Rodriguez, A. M.; Gaspar, J. f.; Martins, C.; Biver, T.; Espino, G.; Leal, J. M.; Garcia, B. Preparation of Organometallic Ruthenium−Arene−Diaminotriazine Complexes as Binding Agents to DNA. *Chem. - Asian J.* **2012**, *7*, 788−801.
(10) Kong, D.; Tian, M.; Guo, L.; Liu, X.; Zhang, S.; Song, Y.; Meng, X.; Wu, S.; Zhang, L.; Liu, Z. Novel iridium(III) iminopyridine complexes: synthetic, catalytic, and in vitro anticancer activity studies. *JBIC, J. Biol. Inorg. Chem.* **2018**, *23*, 819−832.
(11) Alessio, E. Thirty Years of the Drug Candidate NAMI-A and the Myths in the Field of Ruthenium Anticancer Compounds: A Personal Perspective. *Eur. J. Inorg. Chem.* **2017**, *2017*, 1549−1560.
(12) Bijelic, A.; Theiner, S.; Keppler, B. K.; Rompel, A. X-ray Structure Analysis of Indazolium trans-[Tetrachlorobis(1H-indazole)-ruthenate(III)] (KP1019) Bound to Human Serum Albumin Reveals Two Ruthenium Binding Sites and Provides Insights into the Drug Binding Mechanism. *J. Med. Chem.* **2016**, *59*, 5894−5903.
(13) Berndsen, R. H.; Weiss, A.; Abdul, U. K.; Wong, T. J.; Meraldi, P.; Griffioen, A. W.; Dyson, P. J.; Nowak-Sliwinska, P. Combination of ruthenium (II)-arene complex [Ru (η6-p-cymene) Cl2 (pta)]-(RAPTA-C) and the epidermal growth factor receptor inhibitor erlotinib results in efficient angiostatic and antitumor activity. *Sci. Rep.* **2017**, *7*, 43005−43020.
(14) Li, J.; Guo, L.; Tian, Z.; Tian, M.; Zhang, S.; Xu, K.; Qian, Y.; Liu, Z. Novel half-sandwich iridium(iii) imino-pyridyl complexes showing remarkable in vitro anticancer activity. *Dalton Trans.* **2017**, *46*, 15520−15534.
(15) Xu, Z.; Kong, D.; He, X.; Guo, L.; Ge, X.; Liu, X.; Zhang, H.; Li, J.; Yang, Y.; Liu, Z. Mitochondria-targeted half-sandwich rutheniumII diimine complexes: anticancer and antimetastasis via ROS-mediated signalling. *Inorg. Chem. Front.* **2018**, *5*, 2100−2105.
(16) Liu, Z.; Habtemariam, A.; Pizarro, A. M.; Fletcher, S. A.; Kisova, A.; Vrana, O.; Salassa, L.; Bruijnincx, P. C. A.; Clarkson, G. J.; Brabec, V.; Sadler, P. J. Organometallic Half-Sandwich Iridium Anticancer Complexes. *J. Med. Chem.* **2011**, *54*, 3011−3026.
(17) Aird, R.; Cummings, J.; Ritchie, A.; Muir, M.; Morris, R.; Chen, H.; Sadler, P.; Jodrell, D. In vitro and in vivo activity and cross resistance profiles of novel ruthenium (II) organometallic arene complexes in human ovarian cancer. *Br. J. Cancer* **2002**, *86*, 1652−1657.
(18) Soldevila-Barreda, J. J.; Romero-Canelón, I.; Habtemariam, A.; Sadler, P. J. Transfer hydrogenation catalysis in cells as a new approach to anticancer drug design. *Nat. Commun.* **2015**, *6*, 6582−6590.
(19) Hearn, J. M.; Hughes, G. M.; Romero-Canelon, I.; Munro, A. F.; Rubio-Ruiz, B.; Liu, Z.; Carragher, N. O.; Sadler, P. J. Pharmacogenomic investigations of organo-iridium anticancer complexes reveal novel mechanism of action. *Metallomics* **2018**, *10*, 93−107.
(20) Štarha, P.; Habtemariam, A.; Romero-Canelón, I.; Clarkson, G. J.; Sadler, P. J. Hydrosulfide Adducts of Organo-Iridium Anticancer Complexes. *Inorg. Chem.* **2016**, *55*, 2324−2331.
(21) Tian, M.; Li, J.; Zhang, S.; Guo, L.; He, X.; Kong, D.; Zhang, H.; Liu, Z. Half-sandwich ruthenium(ii) complexes containing N^N-chelated imino-pyridyl ligands that are selectively toxic to cancer cells. *Chem. Commun.* **2017**, *53*, 12810−12813.
(22) Sudding, L. C.; Payne, R.; Govender, P.; Edafe, F.; Clavel, C. M.; Dyson, P. J.; Therrien, B.; Smith, G. S. Evaluation of the in vitro anticancer activity of cyclometalated half-sandwich rhodium and iridium complexes coordinated to naphthaldimine-based poly-(propyleneimine) dendritic scaffolds. *J. Organomet. Chem.* **2014**, *774*, 79−85.
(23) Lo, K. K.-W. Luminescent Rhenium(I) and Iridium(III) Polypyridine Complexes as Biological Probes, Imaging Reagents, and Photocytotoxic Agents. *Acc. Chem. Res.* **2015**, *48*, 2985−2995.
(24) Chen, M. H.; Wang, F. X.; Cao, J. J.; Tan, C. P.; Ji, L. N.; Mao, Z. W. Light-Up Mitophagy in Live Cells with Dual-Functional Theranostic Phosphorescent Iridium(III) Complexes. *ACS Appl. Mater. Interfaces* **2017**, *9*, 13304−13314.
(25) Huang, H.; Zhang, P.; Yu, B.; Chen, Y.; Wang, J.; Ji, L.; Chao, H. Targeting Nucleus DNA with a Cyclometalated Dipyridophenazineruthenium(II) Complex. *J. Med. Chem.* **2014**, *57*, 8971−8983.
(26) Cao, J. J.; Tan, C. P.; Chen, M. H.; Wu, N.; Yao, D. Y.; Liu, X. G.; Ji, L. N.; Mao, Z. W. Targeting cancer cell metabolism with mitochondria-immobilized phosphorescent cyclometalated iridium-(iii) complexes. *Chem. Sci.* **2017**, *8*, 631−640.
(27) Liu, C.; Yang, C.; Lu, L.; Wang, W.; Tan, W.; Leung, C. H.; Ma, D. L. Luminescent iridium(iii) complexes as COX-2-specific imaging agents in cancer cells. *Chem. Commun.* **2017**, *53*, 2822−2825.
(28) Liu, Z.; Sadler, P. J. Organoiridium Complexes: Anticancer Agents and Catalysts. *Acc. Chem. Res.* **2014**, *47*, 1174−1185.
(29) Song, G.; Guo, L.; Du, Q.; Kong, W.; Li, W.; Liu, Z. Highly active mono and bis-ligated iminopyridyl nickel catalysts for 1-hexene reactions. *J. Organomet. Chem.* **2018**, *858*, 1−7.
(30) Wang, C.; Liu, J.; Tian, Z.; Tian, M.; Tian, L.; Zhao, W.; Liu, Z. Half-sandwich iridium N-heterocyclic carbene anticancer complexes. *Dalton Trans.* **2017**, *46*, 6870−6883.
(31) Zelonka, R. A.; Baird, M. C. Benzene Complexes of Ruthenium(II). *Can. J. Chem.* **1972**, *50*, 3063−3072.
(32) Cheung, F. K.; Lin, C.; Minissi, F.; Crivillé, A. L.; Graham, M. A.; Fox, D. J.; Wills, M. An Investigation into the Tether Length and Substitution Pattern of Arene-Substituted Complexes for Asymmetric Transfer Hydrogenation of Ketones. *Org. Lett.* **2007**, *9*, 4659−4662.
(33) Guo, L.; Jing, X.; Xiong, S.; Liu, W.; Liu, Y.; Liu, Z.; Chen, C. Influences of Alkyl and Aryl Substituents on Iminopyridine Fe(II)- and Co(II)-Catalyzed Isoprene Polymerization. *Polymers* **2016**, *8*, 389−400.
(34) He, L.; Li, Y.; Tan, C.-P.; Ye, R. R.; Chen, M. H.; Cao, J. J.; Ji, L. N.; Mao, Z. W. Cyclometalated iridium(iii) complexes as lysosome-targeted photodynamic anticancer and real-time tracking agents. *Chem. Sci.* **2015**, *6*, 5409−5418.
(35) Wang, F. X.; Chen, M. H.; Lin, Y. N.; Zhang, H.; Tan, C. P.; Ji, L. N.; Mao, Z. W. Dual Functions of Cyclometalated Iridium(III) Complexes: Anti-Metastasis and Lysosome-Damaged Photodynamic Therapy. *ACS Appl. Mater. Interfaces* **2017**, *9*, 42471−42481.
(36) Sanchez-Cano, C.; Romero-Canelón, I.; Yang, Y.; Hands-Portman, I. J.; Bohic, S.; Cloetens, P.; Sadler, P. J. Synchrotron X-Ray Fluorescence Nanoprobe Reveals Target Sites for Organo-Osmium Complex in Human Ovarian Cancer Cells. *Chem. - Eur. J.* **2017**, *23*, 2512−2516.
(37) Wang, X.; Zhu, M.; Gao, F.; Wei, W.; Qian, Y.; Liu, H.-K.; Zhao, J. Imaging of a clickable anticancer iridium catalyst. *J. Inorg. Biochem.* **2018**, *180*, 179−185.
(38) Tian, Z.; Li, J.; Zhang, S.; Xu, Z.; Yang, Y.; Kong, D.; Zhang, H.; Ge, X.; Zhang, J.; Liu, Z. Lysosome-Targeted Chemotherapeutics: Half-Sandwich Ruthenium(II) Complexes That Are Selectively Toxic to Cancer Cells. *Inorg. Chem.* **2018**, *57*, 10498−10502.
(39) Li, C.; Yu, M.; Sun, Y.; Wu, Y.; Huang, C.; Li, F. A Nonemissive Iridium(III) Complex That Specifically Lights-Up the Nuclei of Living Cells. *J. Am. Chem. Soc.* **2011**, *133*, 11231−11239.
(40) Wang, C.; Wu, C.; Zhou, X.; Han, T.; Xin, X.; Wu, J.; Zhang, J.; Guo, S. Enhancing Cell Nucleus Accumulation and DNA Cleavage Activity of Anti-Cancer Drug via Graphene Quantum Dots. *Sci. Rep.* **2013**, *3*, 2852−2859.
(41) Liu, Z. C.; Wang, B. D.; Li, B.; Wang, Q.; Yang, Z. Y.; Li, T. R.; Li, Y. Crystal structures, DNA-binding and cytotoxic activities studies of Cu(II) complexes with 2-oxo-quinoline-3-carbaldehyde Schiff-bases. *Eur. J. Med. Chem.* **2010**, *45*, 5353−5361.
(42) Raja, D. S.; Bhuvanesh, N. S. P.; Natarajan, K. A novel water soluble ligand bridged cobalt(ii) coordination polymer of 2-oxo-1,2-dihydroquinoline-3-carbaldehyde (isonicotinic) hydrazone: evaluation of the DNA binding, protein interaction, radical scavenging and anticancer activity. *Dalton Trans.* **2012**, *41*, 4365−4377.
(43) Geldmacher, Y.; Rubbiani, R.; Wefelmeier, P.; Prokop, A.; Ott, I.; Sheldrick, W. S. Synthesis and DNA-binding properties of apoptosis-inducing cytotoxic half-sandwich rhodium (III) complexes

DOI: 10.1021/acs.inorgchem.8b02161
Inorg. Chem. XXXX, XXX, XXX−XXX

with methyl-substituted polypyridyl ligands. *J. Organomet. Chem.* **2011**, *696*, 1023−1031.
(44) Singh, S. K.; Joshi, S.; Singh, A. R.; Saxena, J. K.; Pandey, D. S. DNA binding and topoisomerase II inhibitory activity of water-soluble ruthenium (II) and rhodium (III) complexes. *Inorg. Chem.* **2007**, *46*, 10869−10876.
(45) Gupta, R. K.; Kumar, A.; Paitandi, R. P.; Singh, R. S.; Mukhopadhyay, S.; Verma, S. P.; Das, P.; Pandey, D. S. Heteroleptic arene Ru(ii) dipyrrinato complexes: DNA, protein binding and anti-cancer activity against the ACHN cancer cell line. *Dalton Trans.* **2016**, *45*, 7163−7177.
(46) Meier, S. M.; Kreutz, M. S. D.; Winter, L.; Cseh, M. S. K.; Weiss, M. S. T.; Bileck, A.; Alte, M. S. B.; Mader, J. C.; Jana, M. S. S. An Organoruthenium Anticancer Agent Shows Unexpected Target Selectivity For Plectin. *Angew. Chem., Int. Ed.* **2017**, *56*, 8267−8271.
(47) Pettinari, R.; Marchetti, F.; Petrini, A.; Pettinari, C.; Lupidi, G.; Smoleński, P.; Scopelliti, R.; Riedel, T.; Dyson, P. J. From Sunscreen to Anticancer Agent: Ruthenium(II) Arene Avobenzone Complexes Display Potent Anticancer Activity. *Organometallics* **2016**, *35*, 3734−3742.
(48) Paul, B. K.; Guchhait, N. A spectral deciphering of the binding interaction of an intramolecular charge transfer fluorescence probe with a cationic protein: thermodynamic analysis of the binding phenomenon combined with blind docking study. *Photochem. Photobiol. Sci.* **2011**, *10*, 980−991.
(49) Devagi, G.; Dallemer, F.; Kalaivani, P.; Prabhakaran, R. Organometallic ruthenium(II) complexes containing NS donor Schiff bases: Synthesis, structure, electrochemistry, DNA/BSA binding, DNA cleavage, radical scavenging and antibacterial activities. *J. Organomet. Chem.* **2018**, *854*, 1−14.
(50) Ganeshpandian, M.; Palaniandavar, M.; Muruganantham, A.; Ghosh, S. K.; Riyasdeen, A.; Akbarsha, M. A. Ruthenium(II)−arene complexes of diimines: Effect of diimine intercalation and hydrophobicity on DNA and protein binding and cytotoxicity. *Appl. Organomet. Chem.* **2018**, *32*, 4154−4170.
(51) Umadevi, C.; Kalaivani, P.; Puschmann, H.; Murugan, S.; Mohan, P.; Prabhakaran, R. Substitutional impact on biological activity of new water soluble Ni (II) complexes: Preparation, spectral characterization, X-ray crystallography, DNA/protein binding, antibacterial activity and in vitro cytotoxicity. *J. Photochem. Photobiol., B* **2017**, *167*, 45−57.
(52) Betanzos-Lara, S.; Liu, Z.; Habtemariam, A.; Pizarro, A. M.; Qamar, B.; Sadler, P. J. Organometallic Ruthenium and Iridium Transfer-Hydrogenation Catalysts Using Coenzyme NADH as a Cofactor. *Angew. Chem., Int. Ed.* **2012**, *51*, 3897−3900.
(53) Liu, Z.; Romero-Canelón, I.; Qamar, B.; Hearn, J. M.; Habtemariam, A.; Barry, N. P.; Pizarro, A. M.; Clarkson, G. J.; Sadler, P. J. The potent oxidant anticancer activity of organoiridium catalysts. *Angew. Chem., Int. Ed.* **2014**, *53*, 3941−3946.
(54) Liu, Z.; Deeth, R. J.; Butler, J. S.; Habtemariam, A.; Newton, M. E.; Sadler, P. J. Reduction of Quinones by NADH Catalyzed by Organoiridium Complexes. *Angew. Chem., Int. Ed.* **2013**, *52*, 4194−4197.
(55) Panieri, E.; Santoro, M. M. ROS homeostasis and metabolism: a dangerous liason in cancer cells. *Cell Death Dis.* **2016**, *7*, 2253−2264.
(56) Jiang, Y.; Wang, X.; Hu, D. Furanodienone induces G0/G1 arrest and causes apoptosis via the ROS/MAPKs-mediated caspase-dependent pathway in human colorectal cancer cells: a study in vitro and in vivo. *Cell Death Dis.* **2017**, *8*, 2815−2828.

DOI: 10.1021/acs.inorgchem.8b02161
Inorg. Chem. XXXX, XXX, XXX−XXX